In situ Investigation of Magnetism in Metastable Phases of Levitated $Fe_{83}B_{17}$ During Solidification

D. G. Quirinale,[1] D. Messina,[1] G. E. Rustan,[1] A. Kreyssig,[1,2] R. Prozorov,[1,2] and A. I. Goldman[1,2]
[1]*Department of Physics and Astronomy, Iowa State University, Ames, Iowa 50011, USA*
[2]*Ames Laboratory, USDOE, Iowa State University, Ames, Iowa 50011, USA*
(Received 12 May 2017; revised manuscript received 7 August 2017; published 22 November 2017)

In situ measurements of structure, density, and magnetization on samples of $Fe_{83}B_{17}$ using an electrostatic levitation furnace allow us to identify and correlate the magnetic and structural transitions in this system during its complex solidification process. In particular, we identify magnetic ordering in the metastable $Fe_{23}B_6$/fcc Fe coherently grown structures and primitive tetragonal Fe_3B metastable phase in addition to characterizing the equilibrium Fe_2B phase. Our measurements demonstrate that the incorporation of a tunnel-diode oscillator circuit within an electrostatic levitation furnace enables investigations of the physical properties of high-temperature metastable structures.

DOI: 10.1103/PhysRevApplied.8.054046

I. INTRODUCTION

Thermophysical properties such as density, specific heat, viscosity, surface tension, emissivity, conductivity, and magnetization provide valuable insight into the nature of the metastable solids and liquids and critical data for quantitative modeling of phase selection and solidification. However, metastable phases at high temperature are notoriously difficult to characterize, particularly when environmental contamination is of concern. Nevertheless, the ability to determine *in situ* both the structure and properties of these metastable phases, their formation with composition and temperature, and their role in the formation or inhibition of stable phases at lower temperatures can add tremendously to our understanding of stable phase formation in complex systems.

The Fe-B binary system has been the subject of intense study for decades since it is a constituent of magnetic materials critical to a number of industries [1–3] as well as the essential component of a number of metallic glasses [4,5]. Devitrification experiments on glassy samples have observed an abundance of metastable phases, such as primitive tetragonal (PT) Fe_3B, body-centered tetragonal (bct) Fe_3B, orthorhombic (O) Fe_3B, and cubic $Fe_{23}B_6$. *In situ* studies [6–8] have provided additional insights into the solidification pathways in eutectic $Fe_{83}B_{17}$. In particular, our recent *in situ* high-energy x-ray studies [9,10] of $Fe_{83}B_{17}$ have revealed that this alloy solidifies either directly into the equilibrium Fe_2B + fcc Fe phases or a metastable phase mixture of $Fe_{23}B_6$ + fcc Fe that, subsequently, either transforms to the equilibrium high-temperature phases (Fe_2B + fcc Fe) or persists down to ambient temperature. The same sample undergoing the same heating process and free cooling exhibits both solidification behaviors in sequence with no discernible difference in cooling rates between the different pathways [9,10]. The sequence of solidification products for samples where the metastable $Fe_{23}B_6$ phase persists to ambient temperature is quite complex. For example, the $Fe_{83}B_{17}$ phase is accompanied by the presence of coherently grown fcc Fe which also persists to temperatures well below the allotropic fcc-bcc transition at approximately 1150 K on cooling, and the metastable PT Fe_3B is also observed at lower temperatures.

Given the past emphasis on the magnetic properties of the $Fe_{23}B_6$ phase [11], as well as extensive investigations of the magnetism of fcc Fe structures stabilized on a variety of substrates [12–14], there is considerable interest in the nature and formation of magnetism in these nonequilibrium phases. The complex nature of the solidification, however, requires a probe that is well suited to the challenges of high temperature, the time dependence of the solidification process itself, and the requisite sensitivity to detect the subtle signals of the emergent magnetism. To overcome these challenges, the containerless environment of an electrostatic levitation furnace has been combined with a tunnel-diode oscillating (TDO) circuit adapted for high-temperature processing, enabling precision contactless measurements of dynamic magnetic susceptibility [15,16]. While the TDO method has traditionally been employed as a highly sensitive probe of resistivity, susceptibility, and London penetration depth in the low-temperature regime, here it is adapted for use in high-temperature processing.

Applied concurrently with simultaneous volumetric measurements and correlated with high-energy x-ray diffraction experiments for phase determination, we identify and characterize a number of magnetic transitions during the solidification of $Fe_{83}B_{17}$. Several results including an enhanced magnetic ordering temperature for $Fe_{23}B_6$ are obtained from our measurements.

II. EXPERIMENTAL DETAILS

A. Sample preparation

$Fe_{83}B_{17}$ ingots are prepared by arc melting 99.99% pure Fe from the Toho Zinc Corporation and 99.9999% pure B from Alfa Aesar. A reducing atmosphere is used inside the arc melter to prevent oxidation and facilitate the dissolution of oxide phases in the source material. The produced ingots are then broken into small chunks ranging in size from 30 to 80 mg. These pieces are placed on a polished graphite surface and laser melted several times to form the spheres desired for stable levitation. The first melt is performed under an Airgas forming gas (5% H_2, 95% Ar_2), and the sample, now a molten sphere, is held in the liquid state until the surface is visibly clear of oxide patches. The samples are subsequently briefly melted in high vacuum (approximately 10^{-7} torr) to assist in prelevitation degassing. All materials are carefully massed before and after each processing step to control evaporative mass loss and the associated stoichiometry shift. In addition, a Leco CS-444 carbon determinator is used to measure potential carbon contamination from the graphite substrates. No appreciable difference in carbon content is found between the raw material and the graphite-processed spheres.

B. Electrostatic levitation

The samples are levitated in the Iowa State University Electrostatic Levitation system (ISU ESL), which is described in detail elsewhere [15,16]. The positioning system is based on a pair of orthogonal LEDs casting shadows of the sample on position-sensitive detectors. Combined with a high-speed feedback loop operating at 500 Hz, the sample position can be maintained to within 3–5 μm [15]. Bidirectional sample heating is accomplished using a fiber-coupled laser. Controlled heating and cooling ramps are performed using a proportional-integral-derivative (PID) controller algorithm in the LabVIEW laser-control program at a rate of 2 K/s. All samples are freely cooled through the initial solidification plateau by turning off the laser, with any cooling rates applied once solidification completes, in order to not bias the phase selection process. The data presented here are taken on a 43-mg sample exhibiting approximately 0.1 mg of mass loss through the course of ten heating and cooling cycles. Volumetric measurements are performed in the ISU ESL using a well-established videographic algorithm [16–18] and performed concurrently with the TDO measurements to ensure that the observed magnetic transitions can be correlated consistently with transitions in the x-ray data.

C. Tunnel-diode oscillator

The ISU ESL TDO is described in detail in Refs. [15,16]. Briefly, a copper coil is installed in the bottom electrode of the ESL and connected to a tank circuit driven by a tunnel diode biased to the region of negative differential resistance on its V-I curve. Samples levitating above the coil are inductively coupled to the coil (inductor) of the oscillator circuit, and changes in the sample conductivity and/or magnetization result in a shift of the circuit's resonant frequency $f_0 = (2\pi\sqrt{LC})^{-1}$. In the case where the radius of the sample a is much larger than the classical skin depth δ, this leads to the expression:

$$\frac{\Delta f}{f_0} = \frac{3}{4}\phi\left(1 - \frac{3\delta}{2a}(1+\chi)\right), \tag{1}$$

where Δf is the shift in frequency, f_0 is the resonant frequency of the empty circuit without the sample, ϕ is the sample filling factor, and $\chi = \mu - 1$ is the magnetic susceptibility. In general, the frequency shift is proportional to the total magnetic susceptibility of the sample, which consists of both skin-effect diamagnetism and electronic magnetism—either dia or para depending on the situation. The latter effect originates from the skin-depth layer accessible to the ac excitation field. As we show below, the onset of magnetic ordering can produce frequency shifts of 10^2–10^3 Hz. Any effects of temperature fluctuations of the coil itself are mitigated using the procedure for background subtraction outlined in Ref. [15].

D. High-energy x-ray diffraction

High-energy x-ray diffraction measurements are performed at Beamline 6-ID-D (λ=0.09411 Å, E = 131 keV) at the Advanced Photon Source at Argonne National Laboratory. The samples are levitated in the Washington University Beamline Electrostatic Levitation Chamber, a detailed description of which can be found in Ref. [19], and processed using a similar procedure to the one described in Ref. [10]. A two-dimensional GE Revolution 41-RT amorphous silicon flat-panel detector is used for rapid acquisition of diffraction patterns in transmission geometry, with approximately 88% transmission through the sample. All x-ray data presented here are obtained at one frame per second on a single 46-mg sample. Diffraction patterns are obtained on both cooling and heating so that the phases present can be thoroughly established and correlated with the TDO measurements. No automated temperature control is available, but efforts are made to match the ramp rates used for the TDO study. Gaps in the x-ray data are due to detector memory limits on continuous acquisitions. ImageJ [20] is used to correct diffraction images for dark current and background. Fit2D [21,22] is used to determine detector distance, correct for detector rotation and tilt, and azimuthally integrate the 2D data. GSAS [23] is used for all sequential Rietveld refinements.

III. RESULTS

A. Equilibrium solidification

In Fig. 1, we show the x-ray, volumetric, and TDO data for a cooling and heating cycle, where the $Fe_{83}B_{17}$ sample solidifies into the equilibrium Fe_2B + fcc Fe phases from the melt. Here, the cooling rate is controlled by applying the laser starting 100 K below the solidification plateau, after initial phase selection occurs. Fe_2B is the primary equilibrium phase, accompanied by fcc Fe at high temperature which transforms to bcc Fe near $T = 1150$ K. The transformation of fcc Fe to bcc Fe represents a shift in average volume per Fe atom from 12.188 $Å^3$/atom to 12.238 $Å^3$/atom, which is reflected in the cooling curve in Fig. 1(c) as an expansion at the transition. On heating, the bcc Fe to fcc Fe transition is observed in the x-ray data at 1220 K, and the corresponding volume contraction is seen in Fig. 1(c) at nearly the same temperature.

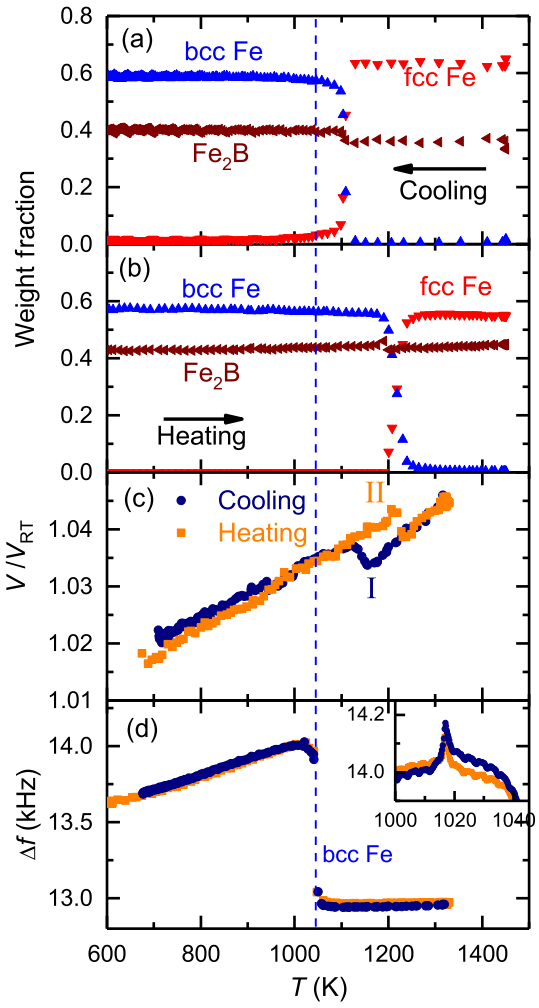

FIG. 1. (a),(b) Results of the Rietveld refinements of the x-ray data. The red triangles represent fcc Fe, blue triangles represent bcc Fe, and the brown triangles represent Fe_2B. Weight fractions in panel (a) are measured on cooling, and those in (b) are measured on heating. (c) Volumetric data taken in the ISU ESL represented as fractional changes from ambient-temperature values. Temperatures labeled as I and II denote the allotropic transition on cooling and heating, respectively. (d) Frequency shift measured by the TDO circuit. The inset displays the peak near 1018 K taken on a similarly sized sample with data taken at a lower cooling and heating rate (approximately 0.25 K/s) for higher resolution. Dark blue circles correspond to cooling, and orange squares represent the subsequent reheat.

The TDO data in Fig. 1(d) exhibit a sizeable frequency shift (proportional to the magnetic susceptibility of the sample) at 1040 K, with a magnitude of 1080 Hz, signifying a large increase in magnetic susceptibility corresponding to the onset of magnetic ordering. This temperature closely matches the known Curie temperature (T_C) for the onset of ferromagnetism for bcc Fe of 1043 K. On heating, a comparable decrease in frequency is observed at the same temperature, signaling the transition from ferromagnetic order below to paramagnetism above T_C. Furthermore, there is a small but persistent peak at 1018 K. The well-established T_C for Fe_2B of 1015 K [24] suggests this feature arises from the ferromagnetic ordering of Fe_2B. Both the shape and the magnitude of this feature, however, are quite different from the steplike TDO frequency shift observed for the ferromagnetic ordering of bcc Fe.

Extensive investigations of the TDO response to magnetic transitions have determined that large, steplike increases in the frequency shift are associated with the onset of itinerant ferromagnetism [25], consistent with the itinerant magnetism in bcc Fe. Alternatively, ferromagnetic transitions in local moment systems demonstrate small, sharp peaks in the frequency shift [25,26] due to critical fluctuations. The shape and small frequency shift of the Fe_2B transition with respect to its weight fraction is consistent with past evidence for local moment magnetism in Fe_2B [27]. These results further demonstrate that the nature of the ordering (local vs itinerant) in magnetic materials, as well as the ordering temperature itself, may be elucidated through TDO measurements.

B. Metastable solidification

We now turn to our measurements displayed in Fig. 2 for a cooling and heating cycle where the $Fe_{83}B_{17}$ sample solidifies into the metastable $Fe_{23}B_6$ + fcc Fe phases from the melt. This cycle is performed subsequent to the cycle presented in Fig. 1, on the same sample. To ensure the capture of the kinetics of the metastable phase transitions with temperature, all of these data are taken while free cooling the sample from high temperature, as applying the laser to control the cooling rate after solidification often results in a metastable to equilibrium transformation. Figures 2(a) and 2(b) are again the calculated weight fractions from the Rietveld refinements of the x-ray data during cooling and heating, respectively, and are consistent with our previous results [9,10].

On cooling, the fcc Fe to bcc Fe transformation is suppressed to much lower temperature, commencing at

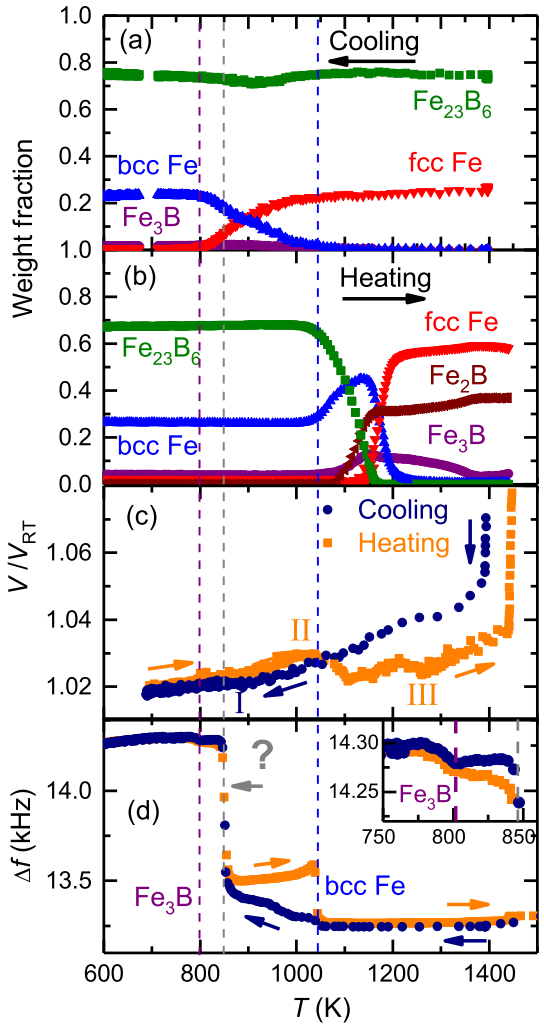

FIG. 2. (a),(b) Results of Rietveld refinements on x-ray data. Green squares represent $Fe_{23}B_6$, red triangles pointing down represent fcc Fe, blue triangles pointing up represent bcc Fe, brown triangles pointing left represent Fe_2B, and purple circles represent Fe_3B. Fractions in (a) are measured on cooling and those in (b) are measured on heating. (c) Sample volume as compared to an ambient-temperature measurement. Points I–III are temperatures corresponding to transitions as described in the text. (d) The measured frequency shift in the TDO. The inset presents a detailed view of the signal near 790 K.

approximately 1050 K and is quite broad in temperature. A small weight fraction of the metastable PT Fe_3B precipitates but does not continue to grow beyond approximately 5% of the sample weight. Rather than the sharp change in the volumetric data [Fig. 1(c)] that we describe above, the allotropic transition is reflected in Fig. 2(c) as an inflection midway through the fcc Fe to bcc Fe transition region labeled I. On heating, the transformation from $Fe_{23}B_6$ to Fe_2B commences near 1050 K, accompanied by an increase in the weight fraction of Fe_3B and bcc Fe, consistent with the contraction in the volumetric data at point II in Fig. 2(c). The allotropic transition from bcc Fe to fcc Fe occurs slightly higher, between 1150 and 1200 K in the x-ray data, and beginning at point III near 1200 K in the volume data, a discrepancy most likely due to differing heating rates between data sets. Finally, as the sample is heated above approximately 1375 K, the metastable Fe_3B transforms to Fe_2B and fcc Fe.

Figure 2(d) displays the corresponding TDO data for this solidification pathway. In contrast to the data shown in Fig. 1(d), on cooling, there is no evidence of a sharp ferromagnetic transition at 1040 K, consistent with the absence of the bcc Fe at that temperature in the x-ray data. Rather, the TDO frequency shift exhibits a slow rise beginning at 1040 K, concomitant with the slow increase in the weight fraction of ferromagnetically ordered bcc Fe as the temperature decreases. This signal can be associated with the transformation to the bcc Fe phase. At $T = 850$ K, there is a large increase in the signal TDO frequency, again indicating a transition to a ferromagnetically ordered state. There is no known T_C among the iron borides at 850 K, with the closest belonging to bct Fe_3B at 786 K and (O) Fe_3B at 897 K [28]. The transition at 850 K is followed by a small, reversible signal at 790 K, close to the reported T_C of bct Fe_3B, though far from the reported T_C of PT Fe_3B. This low-magnitude transition of 25 Hz could be associated with the small fraction of the sample occupied by Fe_3B ($< 5\%$). Both signals are again present on heating, where bcc Fe shows a ferromagnetic to paramagnetic transition at 1040 K, with a magnitude reflecting the low weight fraction relative to that in the equilibrium solidification. The consistency of the bcc Fe transition at 1040 K, with a magnitude of frequency shift correspondingly related to the phase fraction of the bcc Fe present, suggests that it is the only signal associated with the phase and cannot explain the behavior observed at 850 K.

Figure 3 corresponds to an anneal subsequent to the cooling cycle shown in Fig. 2(d). The sample is heated to

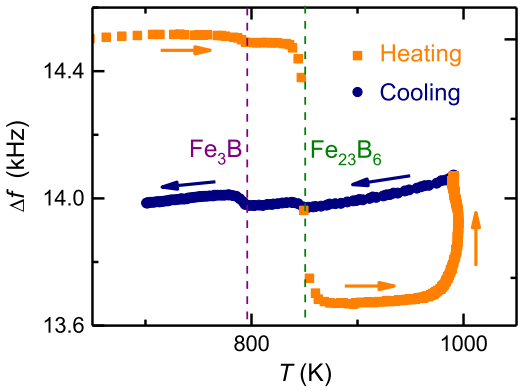

FIG. 3. TDO output from an anneal following the solidification displayed in Figs. 2(c) and 2(d), where the sample is heated to the temperature region where $Fe_{23}B_6$ transforms to Fe_2B + bcc Fe + Fe_3B. Orange squares represent the initial heat and 8-min anneal at 990 K, while blue circles represent the subsequent cool.

approximately 990 K, where the x-ray diffraction results show the beginning of a transformation from $Fe_{23}B_6$ to $Fe_2B + Fe_3B +$ bcc Fe, and held for 8 min before cooling. The volume data obtained simultaneous to the TDO measurement reveals a volume contraction consistent with that seen in heating cycles similar to those present in Fig. 2. On cooling after this anneal, the frequency shift at 850 K has almost disappeared, whereas the signal at 790 K is slightly enhanced. Given the expected increase in Fe_3B content and decrease in $Fe_{23}B_6$, the transition at 790 K must come from Fe_3B, and the signal at 850 K can be associated with ferromagnetic ordering in $Fe_{23}B_6$.

IV. DISCUSSION AND SUMMARY

Studies suggest that the flexibility of the $Fe_{23}B_6$ structure allows for different fractional occupations of the Fe sites and variations in bond lengths [29], resulting in noticeable differences in the magnetic order [30]. A series of investigations by Barinov *et al.* [31] on single-phase $Fe_{23}B_6$ found a range of Curie temperatures from 623 to 701 K related to the Fe site vacancies and B concentration c_B (in %) of the structure by $T_C = (101 + 26.1c_B)$ K. Nominally, $Fe_{23}B_6$ has a c_B of 20.7%, while our recorded T_C (of 850 K) requires a c_B of 28.7%.

Two other explanations for the higher T_C for $Fe_{23}B_6$ seem plausible. The first and most likely is that this higher T_C is a result of the coherent growth of $Fe_{23}B_6$ on large grains of metastable fcc Fe. It is unclear from the Rietveld refinements and raw x-ray data if any of the fcc Fe remains at room temperature, and as past work has demonstrated [10], the overlap of peaks resulting from coherency together with extremely strong texturing make quantitative measurements of the fcc Fe and $Fe_{23}B_6$ fractions challenging. However, the nature of the coherent stabilization might imply a kinetic barrier to further transformation at low temperature, leaving some small grains of fcc Fe throughout the sample.

If some fcc Fe is still indeed present at ambient temperatures, the possibility remains that this signal comes from stabilized fcc Fe clusters. There have been numerous efforts to characterize magnetic ordering in thin films of fcc Fe grown on Cu substrates [32] or in Cu [33] or Cu-Au [34] matrices. While fcc Fe is antiferromagnetic in the ground state, with a Néel temperature of 70 K [35], metastable low-temperature fcc Fe growth is predicted to exhibit a sensitive dependence on its lattice parameter varying from low-spin to high-spin ferromagnetism between 3.57 and 3.62 Å [36,37]. The lowest temperature at which we obtain a reliable lattice parameter of fcc Fe during the most recent course of work with the BESL yields 3.628 Å at 850 K. This implies any stabilized fcc Fe could be within the predicted high-spin regime.

The work performed by combination of x-ray diffraction, volume thermal expansion, and TDO susceptibility measurements paints a clear picture of magnetic transitions in the system. The equilibrium solidification displays the signature of ferromagnetic transitions in bcc Fe and what appears to be a primarily local moment ferromagnet Fe_2B. Among the metastable phases, a transition at 790 K is ascribed to Fe_3B. A transition at 850 K can be safely attributed to a high-Curie-temperature phase resulting from $Fe_{23}B_6$ coherently grown with fcc Fe. This study provides an excellent example of the capacity of containerless instrumentation to map the magnetic phase diagram of sensitive nonequilibrium phases and high-temperature materials.

ACKNOWLEDGMENTS

This study is based upon work supported by the National Science Foundation under Grant No. DMR-1308099. The work at Ames Laboratory is supported by the U.S. Department of Energy, Basic Energy Sciences, of Materials Science and Engineering Division, under Contract No. DE-AC02-07CH11358. The authors wish to acknowledge the assistance of K. F. Kelton, C. Pueblo, S. Saunders, R. Ashcraft, and D. S. Robinson with the high-energy x-ray measurements, and L. Jones and M. Besser at the Materials Preparation Center at the Ames Laboratory for providing the samples in this study.

[1] J. J. Croat, J. F. Herbst, R. W. Lee, and F. E. Pinkerton, PrFe and NdFe based materials: A new class of high performance permanent magnets, J. Appl. Phys. **55**, 2078 (1984).
[2] D. Brown, B. M. Ma, and Z. Chen, Developments in the processing and properties of NdFeB-type permanent magnets, J. Magn. Magn. Mater. **248**, 432 (2002).
[3] D. Givord, H. S. Li, and J. M. Moreau, Magnetic properties and crystal structure of $Nd_2Fe_{14}B$, Solid State Commun. **50**, 497 (1984).
[4] T. Kemeny, I. Vincze, B. Fogarassy, and S. Arajs, Structure and crystallization of Fe-B metallic glasses, Phys. Rev. B **20**, 476 (1979).
[5] M. Palumbo, G. Cacciamani, E. Bosco, and M. Baricco, Thermodynamic analysis of glass formation in Fe-B system, CALPHAD: Comput. Coupling Phase Diagrams Thermochem. **25**, 625 (2001).
[6] L. Battezzati, C. Antonione, and M. Baricco, Undercooling of Ni-B and Fe-B alloys and their metastable phase diagrams, J. Alloys Compd. **247**, 164 (1997).
[7] C. Yang, G. Yang, F. Liu, Y. Chen, N. Liu, D. Chen, and Y. Zhou, Metastable phase formation in eutectic solidification of highly undercooled $Fe_{83}B_{17}$ alloy melt, Physica B (Amsterdam) **373B**, 136 (2006).
[8] A. Mizuno, J. Tamura, S. Kohara, and M. Watanabe, Time-resolved x-ray diffraction study on solidification of Fe-B and Fe-C eutectic alloys, Mater. Sci. Forum **706**, 1702 (2012).
[9] D. G. Quirinale, G. E. Rustan, A. Kreyssig, and A. I. Goldman, Synergistic stabilization of metastable $Fe_{23}B_6$

and γ-Fe in undercooled $Fe_{83}B_{17}$, Appl. Phys. Lett. **106**, 241906 (2015).

[10] D. G. Quirinale, G. E. Rustan, A. Kreyssig, S. Lapidus, M. J. Kramer, and A. I. Goldman, The solidification products of levitated $Fe_{83}B_{17}$ studied by high-energy x-ray diffraction, J. Appl. Phys. **120**, 175104 (2016).

[11] E. F. Kneller and R. Hawig, The exchange-spring magnet: A new material principle for permanent magnets, IEEE Trans. Magn. **27**, 3588 (1991).

[12] E. J. Escorcia-Aparicio, R. K. Kawakami, and Z. Q. Qiu, fcc Fe films grown on a ferromagnetic fcc Co (100) substrate, Phys. Rev. B **54**, 4155 (1996).

[13] S. Muller, P. Bayer, C. Reischl, K. Heinz, B. Feldmann, H. Zillgen, and M. Wuttig, Structural Instability of Ferromagnetic fcc Fe films on Cu (100), Phys. Rev. Lett. **74**, 765 (1995).

[14] D. Bagayoko and J. Callaway, Lattice-parameter dependence of ferromagnetism in bcc and fcc iron, Phys. Rev. B **28**, 5419 (1983).

[15] G. E. Rustan, N. S. Syrison, A. Kreyssig, R. Prozorov, and A. I. Goldman, Noncontact technique for measuring the electrical resistivity and magnetic susceptibility of electrostatically levitated materials, Rev. Sci. Instrum. **83**, 103907 (2012).

[16] G. E. Rustan, Ph.D. thesis, Iowa State University, 2014.

[17] J. C. Bendert, Ph.D. thesis, Washington University, 2013.

[18] R. C. Bradshaw, D. P. Schmidt, J. R. Rogers, K. F. Kelton, and R. W. Hyers, Machine vision for high-precision volume measurement applied to levitated containerless material processing, Rev. Sci. Instrum. **76**, 125108 (2005).

[19] N. A. Mauro and K. F. Kelton, A highly modular beamline electrostatic levitation facility, optimized for *in situ* high-energy x-ray scattering studies of equilibrium and supercooled liquids, Rev. Sci. Instrum. **82**, 035114 (2011).

[20] C. A. Schneider, W. S. Rasband, and K. W. Eliceiri, NIH IMAGE to IMAGEJ: 25 years of image analysis, Nat. Methods **9**, 671 (2012).

[21] A. P. Hammersley, European Synchrotron Radiation Facility Internal Report No. ESRF97HA02T, 1997.

[22] A. P. Hammersley, S. O. Svensson, and A. Thompson, Calibration and correction of spatial distortions in 2D detector systems, Nucl. Instrum. Methods Phys. Res., Sect. A **346**, 312 (1994).

[23] A. C. Larson and R. B. Von Dreele, GSAS: General Structure Analysis System, LANSCE, MS-H805 Los Alamos, New Mexico (1994).

[24] K. A. Murphy and N. Hershkowitz, Temperature-dependent hyperfine interactions in Fe_2B, Phys. Rev. B **7**, 23 (1973).

[25] M. D. Vannette, A. S. Sefat, S. Jia, S. A. Law, G. Lapertot, S. L. Bud'ko, P. C. Canfield, J. Schmalian, and R. Prozorov, Precise measurements of radio-frequency magnetic susceptibility in ferromagnetic and antiferromagnetic materials, J. Magn. Magn. Mater. **320**, 354 (2008).

[26] M. D. Vannette, Ph.D. thesis, Iowa State University, 2009.

[27] P. J. Brown and J. L. Cox, Charge and spin density distributions in the ferromagnetic alloy Fe_2B, Philos. Mag. **23**, 705 (1971).

[28] D. Fruchart, P. Chaudouet, R. Fruchart, A. Rouault, and J. P. Senateur, Etudes structurales de composés de type cémentite: Effet de l'hydrogéne sur Fe_3C suivi par diffraction neutronique. Spectrométrie Mössbauer sur $FeCo_2B$ et Co_3B dopés au ^{57}Fe, J. Solid State Chem. **51**, 246 (1984).

[29] V. A. Barinov and V. T. Surikov, Short-range atomic order in the metastable $Fe_{23}B_6$ phase, Phys. Met. Metallogr. **105**, 245 (2008).

[30] C. M. Fang, M. A. Van Huis, M. H. F. Sluiter, and H. W. Zandbergen, Stability, structure and electronic properties of γ-$Fe_{23}C_6$ from first-principles theory, Acta Mater. **58**, 2968 (2010).

[31] V. A. Barinov, V. A. Tsurin, V. I. Voronin, S. I. Novikov, and V. T. Surikov, Mössbauer investigations of the metastable $Fe_{23}B_6$ phase, Phys. Met. Metallogr. **101**, 456 (2006).

[32] C. A. F. Vaz, J. A. C. Bland, and G. Lauhoff, Magnetism in ultrathin film structures, Rep. Prog. Phys. **71**, 056501 (2008), and references therein.

[33] Y. Tsunoda, S. Imada, and N. Kunitomi, Anomalous lattice contraction and magnetism of γ-Fe precipitates in Cu, J. Phys. F **18**, 1421 (1988).

[34] U. Gonser, K. Krischel, and S. Nasu, Ferromagnetic ordering in fcc γ-Fe precipitates in Cu-Au alloys, J. Magn. Magn. Mater. **15**, 1145 (1980).

[35] S. C. Abrahams, L. Cuttman, and J. S. Kasper, Neutron diffraction determination of antiferromagnetism in face-centered cubic (γ) iron, Phys. Rev. **127**, 2052 (1962).

[36] L. T. Kong and B. X. Liu, Correlation of magnetic moment versus spacing distance of metastable fcc structured iron, Appl. Phys. Lett. **84**, 3627 (2004).

[37] L. T. Kong and B. X. Liu, Distinct magnetic states of metastable fcc structured Fe and Fe-Cu alloys studied by *ab initio* calculations, J. Alloys Compd. **414**, 36 (2006).